The Astrophysical Journal, 1007:33 (15pp), 2026 August 10 https://doi.org/10.3847/1538-4357/ae851e

State of Ammonium Hydrosulfide (NH_4SH) Salt on Icy Bodies in the Trans-Neptunian Space

Chaojiang Zhang[1,2], Zesen Wang[1,2], Jia Wang[1,2], Leslie A. Young[3], and Ralf I. Kaiser[1,2]
[1] W. M. Keck Research Laboratory in Astrochemistry, University of Hawaii at Manoa, Honolulu, HI 96822, USA; ralfk@hawaii.edu
[2] Department of Chemistry, University of Hawaii at Manoa, Honolulu, HI 96822, USA
[3] Department of Space Studies, Southwest Research Institute, Boulder, CO 80302, USA
Received 2025 October 22; revised 2026 June 29; accepted 2026 June 30; published 2026 August 4

Abstract

Ammonium hydrosulfide (NH_4SH) is expected to be widespread on trans-Neptunian objects (TNOs), considering the predicted high abundance of hydrogen sulfide (H_2S) in the presolar nebula and the detection of ammonia (NH_3) on TNOs such as Charon and Orcus. However, the laboratory data on the state of this salt on the surfaces of icy bodies in trans-Neptunian space is still scarce. Here, we conduct comprehensive laboratory experimental studies on the formation of NH_4SH salt at low temperature and explore its response to heating and exposure of this salt to proxies of galactic cosmic rays in the form of energetic electrons under trans-Neptunian space conditions. The NH_4SH is prepared by simultaneously depositing H_2S and NH_3 as low-temperature ices (5 K); the high-temperature and low-flux codeposition experiments suggest that the majority of NH_4SH products are likely to form in the gas phase and then condense. The infrared spectra identified a new absorption at 1.98 μm (5053 cm^{-1}), which is correlated with crystallized NH_4SH. Mass spectra indicated that the radiation chemistry of NH_4SH salt can yield a series of products, including hydrazine (N_2H_4), diazene (N_2H_2), molecular hydrogen (H_2), molecular nitrogen (N_2), and high-order sulfanes (H_2S_n, $n > 8$). The data obtained here provide fundamental information for enabling a thorough exploration of NH_4SH salt behaviors on the surface of TNOs, as well as an alternative explanation for the potential carriers of both ammonium (NH_4^+) ions and sulfur depletion in interstellar conditions.

Unified Astronomy Thesaurus concepts: Astrochemistry (75); Trans-Neptunian objects (1705); Surface ices (2117)

1. Introduction

Hydrogen sulfide (H_2S) has been proposed as an essential precursor to form molecular carriers of the 1.8 μm ($\sim$5555 cm^{-1}) band of the Kuiper Belt object (KBO) Arrokoth, as well as having a high abundance in the presolar nebula (M. E. Brown et al. 2011; W. M. Grundy et al. 2020; A. Mahjoub et al. 2021; N. Pinilla-Alonso et al. 2025). Therefore, hydrogen sulfide has the potential to be involved in vital reactions to form sulfur-bearing prebiotic molecules such as the amino acid cystine [$(SCH_2CH(NH_2)CO_2H)_2$], considering its important role in Miller–Urey analog experiments (B. N. Khare & C. Sagan 1971; E. T. Parker et al. 2011). Ammonia (NH_3) has been detected on the surface of icy bodies in the outer solar system, including Charon, Orcus, and Pluto (M. A. Barucci et al. 2008b; F. Merlin et al. 2010; M. E. Brown 2012; C. M. Dalle Ore et al. 2019). The presence of ammonia can affect their surface color when reacting with organic compounds through ionizing radiation exposure (space weathering); this exposure, in turn, produces complex nitrogen-bearing compounds such as ammonium (NH_4^+), amines ($R-NH_2$), and amino acids (M. E. Brown et al. 2011; N. Pinilla-Alonso et al. 2025; C. Zhang et al. 2025a, 2025b). Under terrestrial conditions, mixing these two toxic gases, ammonia and hydrogen sulfide, leads to the formation of ammonium hydrosulfide (NH_4SH) through an acid–base reaction. This proton transfer from hydrogen sulfide to ammonia can also occur at cryogenic extraterrestrial environments, such as cold molecular clouds ($\sim$10 K) and the atmosphere of Jupiter ($\sim$125−170 K) (S. J. Weidenschilling & J. S. Lewis 1973; H. B. Niemann et al. 1998; M. H. Wong et al. 2004; J. Vitorino et al. 2024; K. Slavicinska et al. 2025). Likewise, the ROSINA Double Focusing Mass Spectrometer indicated a high concentration of NH_4SH salt in the cometary dust of comet 67P/Churyumov-Gerasimenko (K. Altwegg et al. 2022). The 67P is thought to originate from the Kuiper Belt—a vast region in the outer solar system carrying millions of primordial icy bodies of the protoplanetary disk (J. X. Luu & D. C. Jewitt 2002). Hence, the state of NH_4SH on the surface of those chilly objects may contain valuable information on the emergence of this salt on 67P and even the evolution of our solar system. In addition, the thermal and radiation chemistry of this salt can also provide an alternative interpretation of the interstellar sulfur depletion, the origin of ammonium (NH_4^+) toward young stellar objects, and ammonia's low abundance in some outer solar system objects, for example, Pluto (D. P. Ruffle et al. 1999; W. A. Schutte & R. K. Khanna 2003; J. R. Goicoechea et al. 2006; P. D. Tribbett & M. J. Loeffler 2024). Therefore, it is essential to systematically study the thermal and radiation chemistry of NH_4SH under relevant extraterrestrial conditions.

Several previous laboratory studies on NH_4SH ices have been conducted under conditions relevant to the atmosphere of giant planets and ice-covered interstellar grains. M. J. Loeffler et al. (2015) investigated the formation and potential compounds in the coloring of Jupiter's clouds via laboratory simulated experiments. These studies suggested that pure NH_4SH salt exists in the crystalline phase above 155 K and sublimes at 170 K. The proton (H^+) irradiation can disturb the crystalline phase and produce NH_3 and long-chained sulfur-containing species. Those radiolysis products can notably

increase the spectral slope of the ultraviolet-visible (UV–vis) reflectance spectrum of unirradiated ices and thus are proposed to be important contributors to the Great Red Spot of Jupiter (L. A. Lebofsky & M. B. Fegley 1976; M. J. Loeffler et al. 2016; M. J. Loeffler & R. L. Hudson 2018). Under simulated molecular cloud environments, J. Vitorino et al. (2024) studied the reactivity and desorption of NH_4SH and found that the ratio of H_2S to carbonyl sulfide (OCS) from the Nautilus gas-grain model with this salt shows better agreement with the observed results for IRAS 16293-2422B. This is because the addition of NH_4SH can enhance the abundance of H_2S in the model, inferring its pivotal role in molecular evolution during the star formation period. Recently, K. Slavicinska et al. (2025) studied the spectroscopic characteristics of NH_4SH formed through the codeposition of H_2S and NH_3 with and without water, obtaining the apparent band strengths of NH_4^+ and SH^- ions. However, the laboratory research on the state of NH_4SH salt under the surface conditions of icy bodies in the trans-Neptunian space is still scarce.

In the present work, we conduct a comprehensive laboratory-simulated experimental study on the NH_4SH salt formed from the codeposition of H_2S and NH_3 at 5 K, followed by heating, and exposure to high energy electrons (5 keV) at 10 and 40 K. The simulated space weathering experiments mimic the effects of secondary electrons generated in the track of galactic cosmic rays (GCRs) penetrating the icy surface of trans-Neptunian objects (TNOs) (W. Zheng et al. 2009; C. J. Bennett et al. 2014; C. Zhang et al. 2025b). The irradiation temperature reflects the typical surface temperatures of TNOs between 10 and 50 K (L. A. Young et al. 2020; S. M. Menten et al. 2022). The infrared spectra identify a new detectable peak at 1.98 μm (5053 cm^{-1}) that correlates with the crystalline state of NH_4SH. Mass spectra indicate that the radiation chemistry of NH_4SH salt under TNO surface conditions can yield a series of products: hydrazine (N_2H_4), diazene (N_2H_2), molecular hydrogen (H_2), molecular nitrogen (N_2), and sulfanes (H_2S_n, $n > 8$). The data obtained here provide fundamental information for enabling a thorough exploration of the behaviors of the NH_4SH on the surface of icy bodies in the outer solar system and afford an alternative explanation for the origin of the 6.85 μm ($\sim$1460 cm^{-1}) band as found toward young stellar objects, and also the sulfur depletion problem in interstellar conditions (W. A. Schutte & R. K. Khanna 2003; A. Herath et al. 2025).

2. Experimental Methods

The experiments were performed in an ultrahigh vacuum (UHV) chamber at a background pressure of $\sim 3 \times 10^{-11}$ Torr, which has been described in detail elsewhere (M. J. Abplanalp et al. 2016; A. M. Turner & R. I. Kaiser 2020). A polished silver wafer is interfaced to an oxygen-free high-conductivity (OFHC) copper target through a couple of layers of indium foil. This copper target is connected to a two-stage closed-cycle helium refrigerator (CTI-Cryogenics Cryodyne 1020, compressor: CTI-Cryogenics 9600), which can provide a continuous cryogenic temperature monitored by a silicon diode sensor (Lakeshore DT-470); this temperature was regulated in the range of 5–320 K by a programmable temperature controller (Lakeshore 336). Once the substrate is cooled down to 5.0 ± 0.3 K, hydrogen sulfide (H_2S, > 99.5%, Sigma-Aldrich) and ammonia (NH_3, > 99.9992%, Matheson) were deposited onto the low-temperature surface via two glass capillary arrays connected with two leak valves, respectively.

Table 1
Data Were Applied to Calculate the Irradiation Dose in the Deposited Hydrogen Sulfide and Ammonia (H_2S-NH_3) Ice Mixtures

Parameter[a]	Value
Initial kinetic energy of the electrons, E_{init} (keV)	5
Ices	H_2S-NH_3
Irradiation current, I (nA)	1330 ± 120
Irradiation duration, t (s)	36,000
Total number of electrons	3.01×10^{17}
Average penetration depth, l (nm)[a]	251 ± 30
Average kinetic energy of backscattered electrons, E_{bs} (eV)[a]	3671 ± 320
Fraction of backscattered electrons, f_{bs}^a	0.46 ± 0.03
Average kinetic energy of transmitted electrons, $E_{\rm trans}$ (eV)[a]	0
Fraction of transmitted electrons, $f_{\rm trans}^a$	0
Irradiated area, A (cm^2)	1.00 ± 0.05
Dose (eV amu^{-1})	82 ± 10

Note.
[a] Parameters are obtained from CASINO software v2.4.2.

The leak pressures for the two gas molecular flows are controlled to the same value of $(1 \pm 0.1) \times 10^{-8}$ Torr by two variable leak valves, taking about 8 minutes. The thicknesses of the deposited ices are estimated to be 850 $\pm$ 50 nm by monitoring the interference pattern of a helium-neon laser (CVI Melles-Griot, 25-LHP-213, 632.8 nm) at a 4° angle of incidence (O. S. Heavens 1955; A. M. Turner et al. 2015). Note that estimating the thickness of ice requires the refractive index (n). However, there is no available refractive index data for the ice mixtures of H_2S, NH_3, and NH_4SH at low temperatures. Therefore, this study uses an average refractive index of H_2S (1.407 ± 0.005) and NH_3 (1.33 ± 0.01), which is consistent with previous reports (J. R. Ferraro et al. 1980; M. J. Loeffler et al. 2015; R. L. Hudson et al. 2022; Y. Y. Yarnall & R. L. Hudson 2022).

After the deposition, the ice was processed via either of two strategies. One is heating the ice at a rate of 1 K min^{-1} until the species in ices are desorbed; this experiment is designed to understand the thermal response of ices. The second strategy involves first a heating of the ices to 10 or 40 K, and then an isothermal processing by 5 keV electrons (Specs Equation 22/35 electron source) to simulate the secondary electrons formed in the track of GCR penetrating TNO surface or interstellar ices (R. E. Johnson 1991; C. J. Bennett et al. 2005); these experiments study the chemical reactions within the ices under space-weathering conditions. The electron beam has an incidence angle of 70° to the ice surface normal. Utilizing Monte Carlo simulations (CASINO 2.42) (D. Drouin et al. 2007), the electrons penetrate 251 ± 30 nm into the ices on average. The maximum depth of the electrons is calculated to be 595 ± 50 nm, which is less than the ice thickness of 850 ± 50 nm, thus avoiding interaction between electrons and the surface of the silver wafer. The radiation dose is controlled to be 82 $\pm$ 10 eV amu^{-1} (Table 1) by adjusting the radiation current and duration for different samples (A. M. Turner et al. 2021; C. Zhang et al. 2024). The density used for estimating the dose is from averaging that of hydrogen sulfide (0.944 g cm^{-3}) and ammonia (0.68 g cm^{-3}) in the solid state (R. L. Hudson et al. 2022; Y. Y. Yarnall & R. L. Hudson 2022). To enable the comparison between our results and the dose accumulation in the outer solar system, we provide the unit of the deposited dose in eV amu^{-1}, which is widely adopted in the astronomy community (C. J. Bennett et al. 2013; A. Yeghikyan 2017;

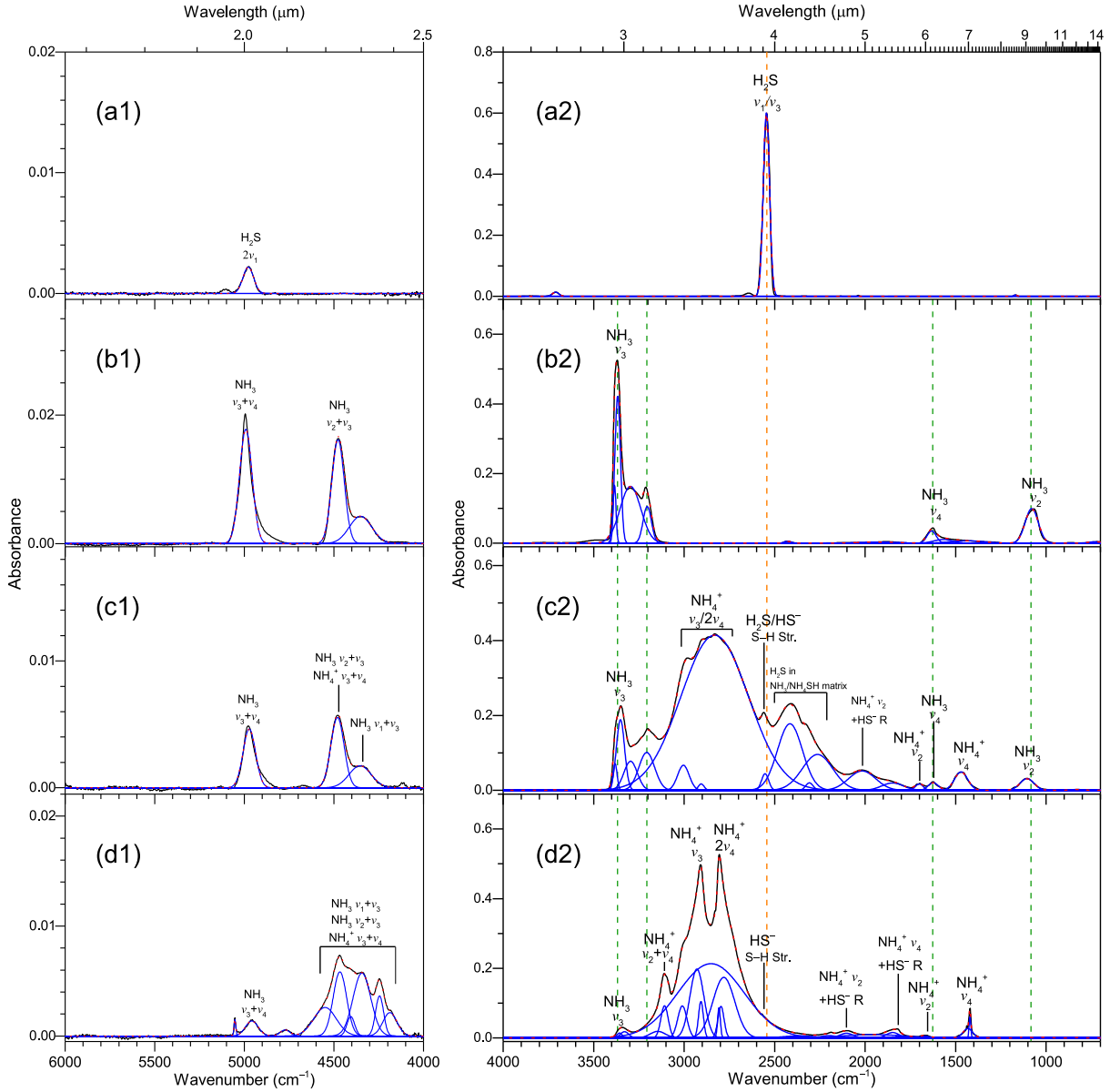

Figure 1. Infrared spectra of (a) hydrogen sulfide (H_2S), (b) ammonia (NH_3), (c) mixed NH_3 and H_2S ices at 5 K, and (d) NH_3 and H_2S ice mixtures heated to 156 K. A suite of broad features observed in the NH_3 and H_2S ice mixtures at 5 K indicates the formation of amorphous ammonium hydrosulfide (NH_4SH) salt. The appearance of narrowing of the salt features at 156 K indicates the formation of crystalline NH_4SH salt. The experimental spectrum is plotted in black, while the deconvoluted peaks are blue, and their sum is shown with the dashed red line. Only noticeable peaks are labeled for clarity, and detailed peak assignments are listed in Table 2.

E. Quirico et al. 2023). This unit can be converted to eV molecule^{-1} used in the astrochemistry community by multiplying the units of eV amu^{-1} by the molecular mass of the reactants, i.e., 16 amu molecule^{-1} for methane (CH_4). The radiation doses applied here reflect exposure times of up to 1800 million years on the surface of TNOs (J. F. Cooper et al. 2003; C. Zhang et al. 2024). After the irradiation, the ices were heated to 320 K at a rate of 1 K min^{-1}. The species within ices were analyzed in situ by a Fourier transform infrared (FTIR) spectrometer (Thermo Fisher Scientific, Nicolet 6700 Spectrometer, liquid-nitrogen-cooled MCT-B detector). The FTIR spectrometer is operated in an absorption-reflection–absorption mode with a reflection angle of 43° between the surface normal of the silver wafer and the infrared beam and monitors the infrared electromagnetic waves in the range of 6000–600 cm^{-1} with a resolution of 4 cm^{-1}. Each infrared spectrum is collected for 2 minutes (220 scans) to minimize the influence of noise signals. A reference spectrum is collected before depositing the ices and subtracted during the collection of infrared spectra. The sublimed species during the temperature-programmed desorption (TPD) phase were also monitored by an electron impact quadrupole mass spectrometer (QMS; Extrel, 5221) in the residual gas analyzer (RGA) model operating at 70 eV with an emission current of 2 mA.

3. Results and Discussion

3.1. Heating of NH_4SH

Figure 1 shows the infrared spectrum of H_2S and NH_3 codeposition in the leak pressure ratio of 1:1 at 5 K from 6000 to 700 cm^{-1}; a second spectrum reveals the heated ices at 156 K; and also presents spectra of pure H_2S and NH_3 at 5 K.

Table 2
Infrared Absorptions of Hydrogen Sulfide (H_2S) at 5 K, Ammonia (NH_3) at 5 K, and the Binary Mixtures (H_2S–NH_3) at 5 K and 156 K

5 K			156 K		
H_2S	NH_3	H_2S–NH_3	H_2S–NH_3	Assignment[a]	References[b]
		Position (cm^{-1})			
...	...	...	5053	$\nu_2+\nu_3$ (NH_4^+)+R (HS^-)[a]	This work
...	4995	4977	4954	$\nu_3+\nu_4$ (NH_3)	(1, 2)
4975	...	...	...	$2\nu_1$ (H_2S)	(3, 5)
...	4475, 4350	4479, 4354	4551, 4468, 4406, 4347, 4246, 4188	$\nu_2+\nu_3$ (NH_3)/$\nu_1+\nu_2$ (NH_3)/$\nu_3+\nu_4$ (NH_4^+)	(1, 2, 3)
3708	...	3720	...	$\nu_1+\nu_2/\nu_2+\nu_3$ (H_2S)	(3, 5)
...	3370	3351	3341	ν_3 (NH_3)	(1, 2)
...	3297	3295	...	$2\nu_4$ (NH_3)	(1, 2)
...	3212	3200	...	ν_1 (NH_3) or $\nu_2+\nu_4$ (NH_4^+)	(1, 2)
...	...	...	3110	$\nu_2+\nu_4$ (NH_4^+)	(3, 4, 5)
...	...	2980	3010, 2908	ν_3 (NH_4^+)	(3, 4, 5)
...	...	2896, 2865, 2831	2805	$2\nu_4$ (NH_4^+)	(3, 4, 5)
2544	...	2561	2569	ν_1/ν_3 (H_2S) or HS^- stretch	(3, 4, 5)
...	...	2409, 2330	...	H_2S in NH_3/NH_4SH matrix	(5)
...	...	2018	2189, 2104	ν_2 (NH_4^+)+R (HS^-)[a]	(3, 4, 5)
...	...	...	1846, 1822	ν_4 (NH_4^+)+R (HS^-)[a]	(3, 4, 5)
...	...	1698	1665	ν_2 (NH_4^+)	(3, 4, 5)
...	1626	1624	...	ν_4 (NH_3)	(1, 2)
...	...	1467	1438, 1420	ν_4 (NH_4^+)	(3, 4, 5)
1171	...	1175	...	ν_2 (H_2S)	(3, 5)
...	1068	1104	1104	ν_2 (NH_3)	(1, 2)
...	...	828	830	2R (HS^-)[a]	(3, 4, 5)

Notes.
[a] R: lattice mode.
[b] References. (1) W. Zheng & R. I. Kaiser (2007); (2) J. S. Holt et al. (2004); (3) J. Bragin et al. (1977); (4) J. R. Ferraro et al. (1980); (5) K. Slavicinska et al. (2025).

Assignments for the vibration frequencies in these spectra are listed in Table 2. A set of broad features originating from the NH_4SH salt at 5 K is identified; this salt is formed upon the codeposition of H_2S and NH_3, consistent with previous experiments at 10 and 15 K (M. J. Loeffler et al. 2015; K. Slavicinska et al. 2025). When heating the ice to 156 K, the infrared spectrum between 3100 and 2600 cm^{-1} showcases a peak splitting and presents sharp peaks at 5053 and 1419 cm^{-1}, reflecting the crystallization of NH_4SH. In the spectrum at 156 K, the remaining feature of the NH_3 ν_3 mode at 3341 cm^{-1} suggests that some of the NH_3 molecules are still trapped in the heated ices. The peak at 1665 cm^{-1} (NH_4^+ ν_2) reveals the incomplete crystallization of NH_4SH, as this vibration mode of crystalline NH_4SH is inactive for infrared detection (J. Bragin et al. 1977). The observed NH_4SH on the low-temperature surface could originate from a solid reaction within the ice. On the other hand, considering the pressure of $(1 \pm 0.1) \times 10^{-8}$ Torr used here, corresponding to a molecular density on the order of 10^8 molecules cm^{-3}, these salts can also first form in the gas phase and then condense. Three further experiments are conducted and compared with the aforementioned experiment (Figure 2). One is codepositing H_2S and NH_3 at 85 K, with leak pressures of $(1 \pm 0.1) \times 10^{-8}$ Torr for each molecule and a total thickness of 850 ± 50 nm (Figure 2(b)). The H_2S cannot condense at this temperature. The infrared spectrum presents strong characteristic peaks of NH_4SH products without H_2S absorption bands. Furthermore, the band area for NH_4^+ ν_4 at 85 K is measured to be 4.0 ± 0.4 cm^{-1}, very close to that of the codeposition experiment at 5 K (3.8 ± 0.4 cm^{-1}). These findings suggest the NH_4SH products are more likely to be formed in the gas-phase reactions due to no H_2S in ices here. Furthermore, two low-flux codeposition experiments at 5 K were also conducted. In these experiments, the H_2S and NH_3 were controlled in the same leak pressure, and each component is $(2 \pm 0.2) \times 10^{-9}$ Torr (lower flux, Figure 2(c)) and $(4 \pm 0.4) \times 10^{-10}$ Torr (lowest flux, Figure 2(d)). To obtain the same thickness of 850 ± 50 nm, these low-flux experiments took 35 and 180 minutes, respectively. Note that the infrared spectra show more H_2S in Figure 2(c) and more NH_3 in Figure 2(d) because of the long-time deposition-induced uncertainty (e.g., the difference of sticking coefficient and density) in these low-flux experiments. But the spectra in both experiments find a notable reduction in the absorbance of NH_4SH, suggesting that the yield of this salt in the ice is correlated with the vapor flux, and most of them are from a gas formation pathway. However, the specific function between the yield and leak pressure still needs further experiments with various leak pressures. In addition, a couple of the isothermal warming layered ice experiments were also conducted where H_2S was deposited first, followed by NH_3 (Figure A1). Both molecules use the leak pressure of $(1 \pm 0.1) \times 10^{-8}$ Torr. While keeping this ice at 85 K, the sublimation of H_2S enhances its diffusion in ice and increases potential reaction sites. However, the formation of NH_4SH is limited, indicating that the solid reaction pathway at 85 K to produce NH_4SH is not favored. These experiments suggest that most of the NH_4SH on the 5 K substrate in the codeposition experiments at 5 K is likely formed from the gas phase before the condensation.

The absorption at 5053 cm^{-1} was only reported by J. R. Ferraro et al. (1980) without assignment. Multiple infrared spectra during heating of the NH_4SH ices present the

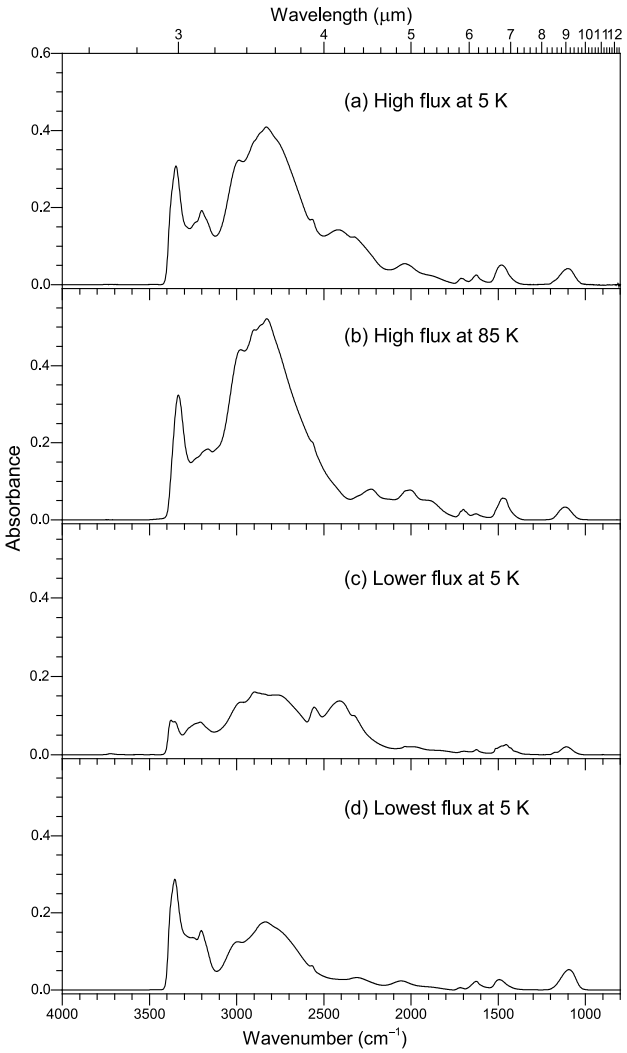

Figure 2. Infrared spectra of the codeposition of H_2S and NH_3 at different temperatures and fluxes. (a) The codeposition at 5 K with each component using leak pressure $(1 \pm 0.1) \times 10^{-8}$ Torr. (b) The codeposition at 85 K with each component using leak pressure $(1 \pm 0.1) \times 10^{-8}$ Torr. (c) The codeposition at 5 K with each component using leak pressure $(2 \pm 0.2) \times 10^{-9}$ Torr. (d) The codeposition at 5 K with each component using leak pressure $(4 \pm 0.4) \times 10^{-10}$ Torr. All the thicknesses were controlled to be 850 ± 50 nm by monitoring He–Ne laser fringes. The H_2S cannot condense at 85 K. Therefore, no H_2S signal was detected in spectrum (b), and the band area for NH_4^+ ν_4 at 85 K is very close to that at 5 K. The lower and lowest flux experiments present a notable reduction in the formation of NH_4SH. These experiments suggest that most of the NH_4SH on the 5 K substrate in the codeposition is likely formed through gas-phase reactions.

same pattern of 5053 cm^{-1} with sharp peaks at 3110 and 1419 cm^{-1} (Figure 3). These three peaks appear at about 136 K, gradually increasing in absorbance as the ices are annealed to about 156 K, then decreasing as the temperature is extended to 200 K. The latter two bands have been reported to be from the crystalline NH_4SH (M. J. Loeffler et al. 2015; K. Slavicinska et al. 2025). Therefore, this peak should also correspond to the crystalline NH_4SH and can be assigned to the combination mode of $\nu_2 + \nu_3 + R$ (HS^-) (J. Bragin et al. 1977). It is important that the peak at 5053 cm^{-1} does not overlap with any bands of the amorphous NH_4SH, thus making it a perfect marker to trace the crystallization process of the NH_4SH salt. Figure 4 presents the evolution of band area at 5053 cm^{-1}. No peak is detected before warming the ices up to 134 K, after which a notable rise is observed, reaching a maximum at 152 K; this is followed by a decline to zero due to the decomposition of crystalline NH_4SH. This evolution reveals a well-defined crystallization pattern for the NH_4SH salt formed in the outer solar system. It is worth noting that these spectra in Figure 3 also present the redshift of the ν_4 mode (6.58 μm band) of amorphous NH_4^+ from 1467 to 1447 cm^{-1} before crystallization, in agreement with K. Slavicinska et al. (2025). Furthermore, the evolution of the band area of this prominent absorption during heating to 200 K is also plotted to characterize the thermal behaviors of the NH_4SH salt (Figure 5). These behaviors represent NH_4SH in both its amorphous and crystalline forms, which differs from Figure 4, which only shows that of crystalline NH_4SH. It first gradually grows between 5 and 40 K and then rapidly increases between 40 and 94 K and remains almost unchanged until 144 K owing to the thermal reaction equilibrium. Note that the NH_4SH salt formed within ices is 50% of that produced from the gas reactions of NH_3 and H_2S co-deposition; this finding is consistent with the results from Figure 2. After 144 K, the band area decreases to zero at about 174 K due to the NH_4SH salt decomposing to H_2S and NH_3 (Figure 6). The integrated area of the peak at $m/z = 36$ is calculated to be 4.4% relative to the signal at $m/z = 32$, corresponding to the natural isotopic distribution of $H_2^{34}S$, which further confirms the decomposition of NH_4SH. The rapid increase of the band area with temperatures from 40 to 90 K suggests a higher thermal reaction rate compared to slower kinetics from 5 to 40 K. Note that M. J. Loeffler et al. (2015) reported a drop-off of this band area near about 140 K for unirradiated NH_4SH, about 40% of its original value, which they attributed to the crystallization process. However, this phenomenon is not observed in the current study. This discrepancy could be due to different heating rates used in both experiments; the previous study employed a slower rate of 0.4 K min^{-1}, while the present study used a rate of 1 K min^{-1}.

3.2. Radiation Effect on NH_4SH

After studying the thermal behaviors of NH_4SH formed in the codeposition of H_2S and NH_3, we conducted the irradiation experiments for the ices at 10 and 40 K. Figures 7 and 8 present infrared spectra before and after the irradiation of the ices at 10 and 40 K, with assignments compiled in Table 3. The spectra of irradiated ices heated to 156 K are also added. In the neat ices, the enhanced infrared peaks of NH_4SH are observed at 40 K due to the thermal reaction between H_2S and NH_3. Upon irradiation, infrared spectra reveal the loss of NH_4SH with increasing radiation dose, but prominent absorptions such as 2988, 2830, and 1474 cm^{-1} are still observed from this salt along with NH_3 and H_2S at the end of the irradiation. Both NH_3 and H_2S exhibit decreases in absorbance during irradiation, indicating radiation-induced degradation. The evolution of the NH_4^+ ν_4 mode during irradiation at 10 and 40 K is plotted in Figure 9(a). At 10 K, 14.5% of NH_4^+ is rapidly destroyed within the first 40 minutes, corresponding to the radiation dose of 5.7 eV amu^{-1}; this fraction gradually reaches 28.5% as the radiation dose increases to 82.1 eV amu^{-1}. At 40 K, the fast decrease of the NH_4^+ ion in the first 40 minutes is similar to that at 10 K, with the loss fraction of 14.5%; however, during the remaining irradiation, this band area shows a subtle increase with a final loss fraction of 6.8%, which may be caused by the competition between thermal reactions and those induced by irradiation. The

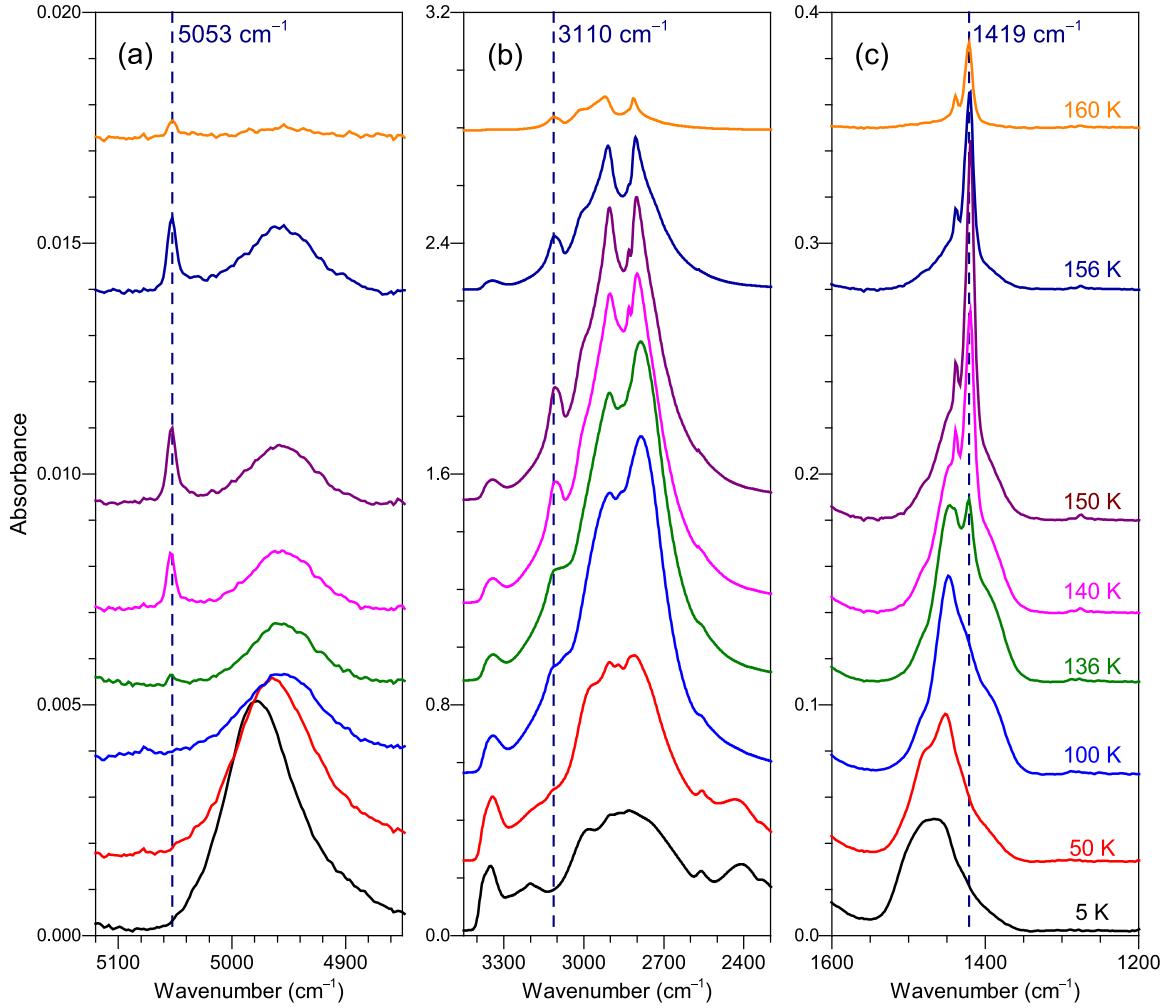

Figure 3. Selected infrared spectra of hydrogen sulfide (H_2S) and ammonia (NH_3) ice mixtures during heating to 200 K. These spectra are displayed in three ranges of (a) 5150–4850 cm^{-1}, (b) 3450–2300 cm^{-1}, and (c) 1600–1200 cm^{-1}. Sharp peaks at 5053 cm^{-1} present the same evolution pattern, with peaks corresponding to crystalline ammonium hydrosulfide (NH_4SH) salt at 3110 and 1419 cm^{-1}. Therefore, this sharp peak is assigned to the crystalline NH_4SH. The lack of overlap between the peak at 5053 cm^{-1} and the bands of amorphous NH_4SH makes it a good tracer for characterizing the behavior of crystalline NH_4SH.

irradiated NH_4SH remains amorphous at 156 K in the TPD phase for both irradiation temperatures (Figures 7(c) and 8(c)). No crystallization of the NH_4SH salt feature is observed, indicating that the prolonged irradiation exposure can hinder its crystallization. Figure 9(b) presents the integrated band area evolution for the NH_4^+ ν_4 mode during heating from 10 and 40 K to 320 K, respectively. These graphs are quite distinct. For ices irradiated at 10 K, the integrated band area exhibits a slight increase from 10 to 70 K, with a sudden drop with the loss fraction of 26.3% from 70 to 90 K, and remains constant between 90 and 120 K, but then subsequently decreases to zero whilst continuing heating. For ices irradiated at 40 K, the band area shows a flat profile from 40 to 116 K, but with an unexpected maximum between 70 and 90 K, and after 120 K declines to zero due to the rapid decomposition of NH_4SH. This different evolution of NH_4^+ in Figure 9(b) can be from a competition between the reversible thermal reaction between NH_3 and H_2S, and the cosublimation event of NH_4^+ and H_2S or NH_3 during their desorption temperature range. The completion degree of radiation chemistry on H_2S and NH_3 at 10 and 40 K is totally different (C. Zhang et al. 2025b), implying different concentrations of residual H_2S and NH_3 in the ice matrix, differing in the evolution of NH_4^+ during warming up.

After commenting on the behavior of NH_4SH during exposure to irradiation, we will now discuss the possible reaction mechanism within the system of NH_4SH embedded in H_2S and NH_3 mixtures initiated by energetic electrons, which simulate the secondary electrons in the track of GCR penetrating ice mantles. The laboratory processing time of TNO ice analogs can be scaled to the corresponding time of exposure experienced by a TNO surface (J. F. Cooper et al. 2003; G. Strazzulla et al. 2003; R. Hudson et al. 2008). This provides the potential to reconstruct the chemical evolution of the NH_4SH salt on the TNO surface triggered by the GCRs exposure and to relate the laboratory scale to the actual solar system timescale. It is necessary to stress that NH_4SH is not a molecule, but rather a salt composed of ammonium (NH_4^+) and bisulfide (HS^-) ions; therefore, the start of radiation chemistry in ices is from a mixture of ice containing NH_4^+, HS^-, NH_3, and H_2S species. For NH_4SH, M. J. Loeffler et al. (2015) proposed a reaction sequence of excitation of the neighbor ion pair to reform NH_3 and H_2S.

$$[NH_4^+ \cdots HS^-] \rightarrow [NH_4^+ \cdots HS^-]_* \rightarrow [NH_3 \cdots H_2S] \rightarrow NH_3 + H_2S. \quad (1)$$

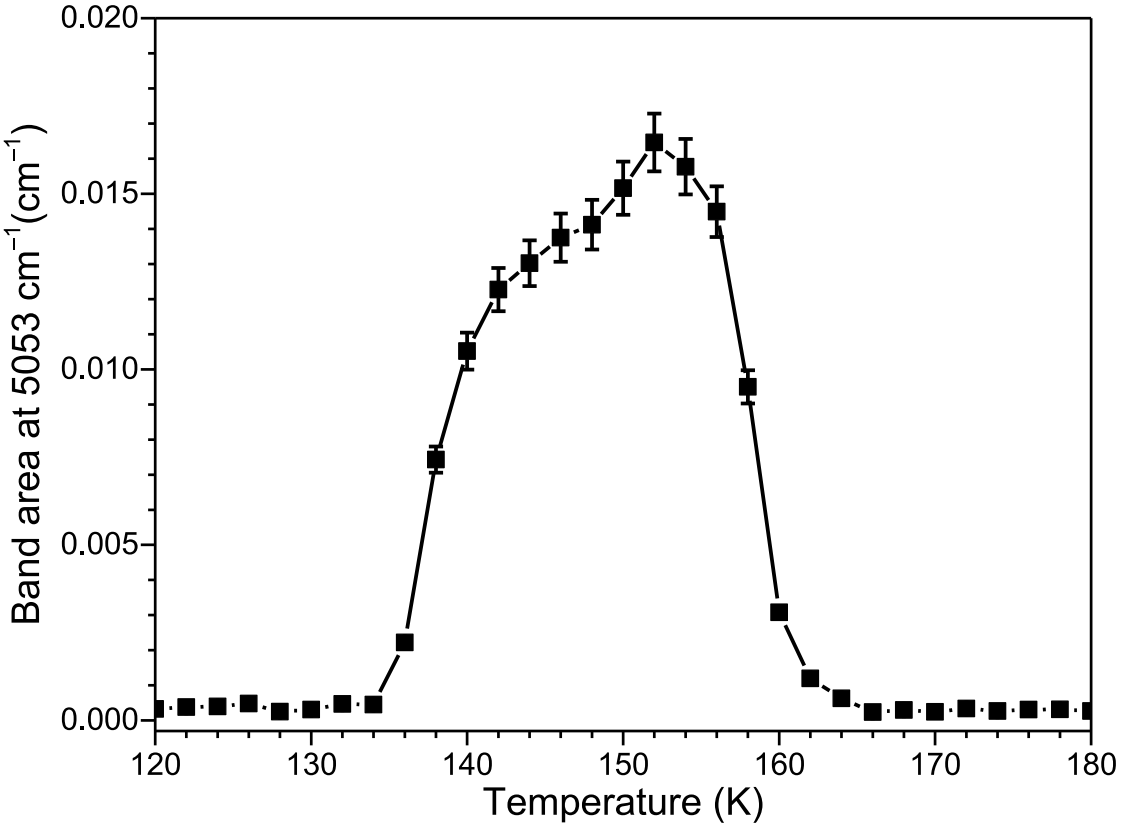

Figure 4. The behavior of only crystalline ammonium hydrosulfide (NH_4SH) salt during warm-up of the hydrogen sulfide (H_2S) and ammonia (NH_3) ice mixtures, which is characterized by the band area of the peak at 5053 cm^{-1}.

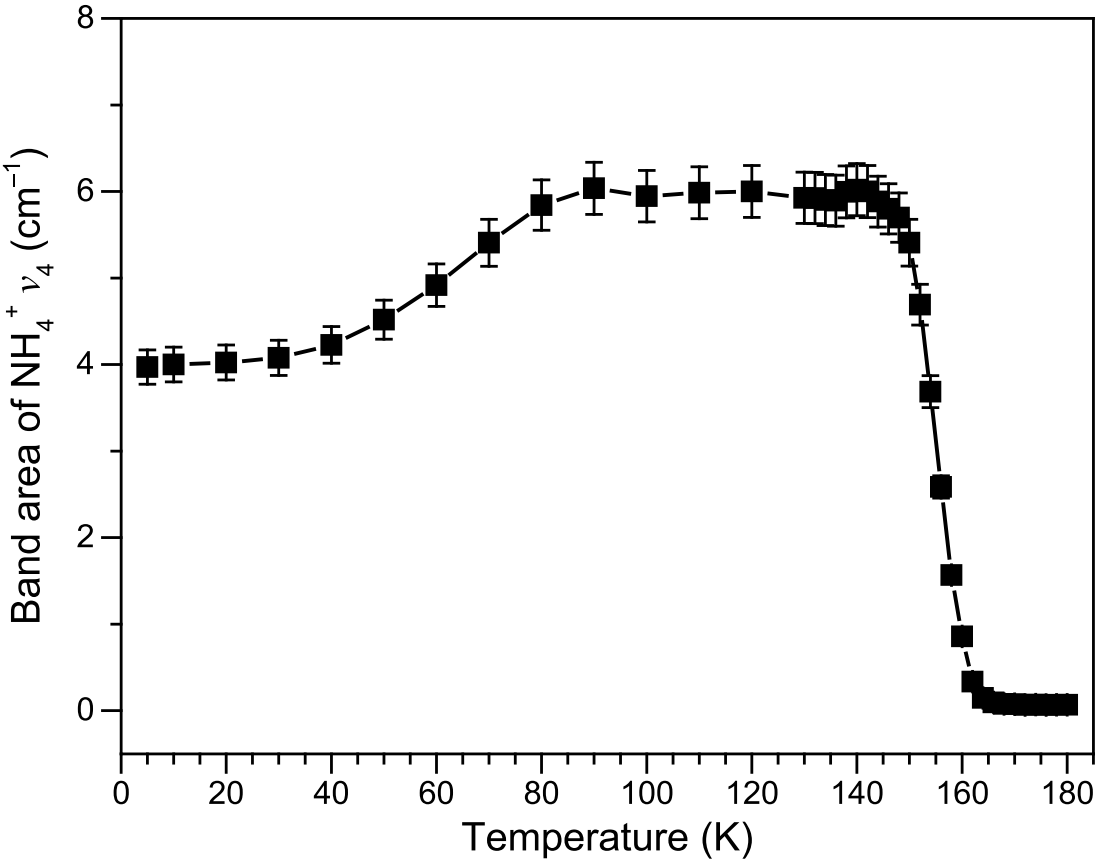

Figure 5. Band area evolution of the ammonium (NH_4^+) ν_4 mode in the amorphous (5–134 K) and mixtures of amorphous and crystalline (134–178 K) ice during warm-up of the hydrogen sulfide (H_2S) and ammonia (NH_3) ice mixtures.

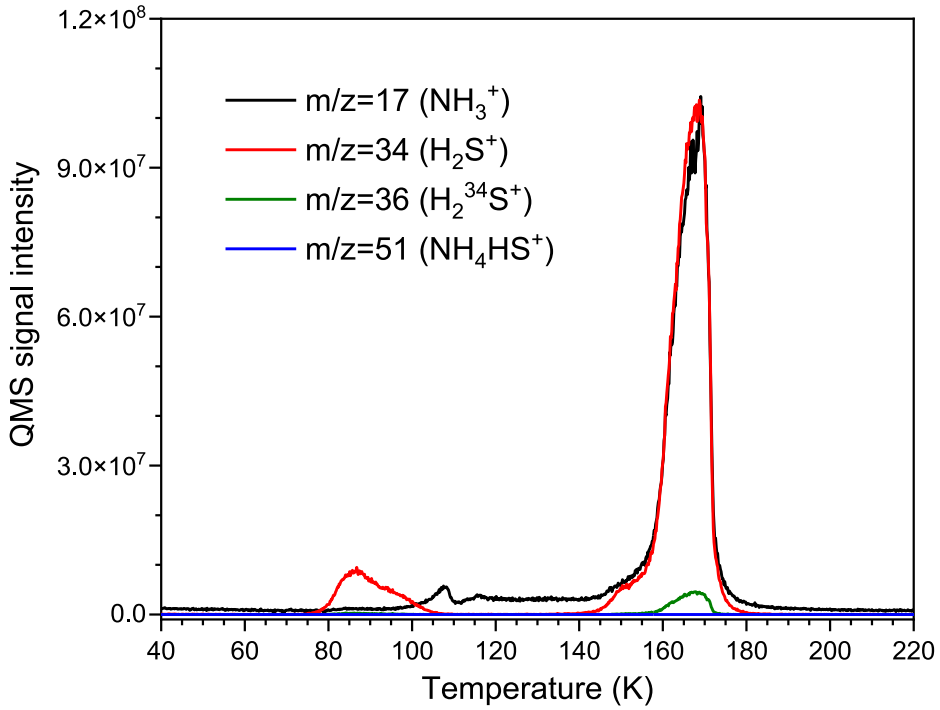

Figure 6. Quadrupole mass spectrometer (QMS) signals of ammonia (NH_3, m/z = 17), hydrogen sulfide (H_2S, m/z = 34; $H_2^{34}S$, m/z = 36), and ammonium hydrosulfide salt (NH_4HS, m/z = 51) during heating the unirradiated hydrogen sulfide and ammonia ice mixture to 220 K.

Table 3
Infrared Absorptions of Hydrogen Sulfide and Ammonia (H_2S-NH_3) Ices before and after Irradiation at 10 and 40 K

Before Irradiation	After Irradiation		Before Irradiation	After Irradiation			
10 K	10 K	156 K	40 K	40 K	156 K		
Position (cm^{-1})						Assignment[a]	References[b]
4979	4971	4973	4977	4967	4966	$\nu_3+\nu_4$ (NH_3)	(1, 2)
4468	4466	4466	4469	4468	4466	$\nu_2+\nu_3$ (NH_3)/$\nu_3+\nu_4$ (NH_4^+)	(1, 2, 3)
4346	4337	4335	4340	4341	4340	$\nu_1+\nu_2$ (NH_3)/$\nu_3+\nu_4$ (NH_4^+)	(1, 2, 3)
4117	4115	4124	4109	4111	4121	ν_4 (NH_4^+)+HS^- stretch	(3)
3383, 3348	3380, 3346	3384, 3345	3378, 3340	3378, 3342	3380, 3341	ν_3 (NH_3)	(1, 2)
3295	3296	3295	3295	3295	3305	$2\nu_4$ (NH_3)	(1, 2)
3200	3197	3197	3196	3196	3194	ν_1 (NH_3) or $\nu_2+\nu_4$ (NH_4^+)	(1, 2, 3, 4, 5)
2988	2992	2992	2977	2988	2988	ν_3 (NH_4^+)	(3, 4, 5)
2830	2831	2829	2824	2830	2827	$2\nu_4$ (NH_4^+)	(3, 4, 5)
2568	2562	2564	2562	2556		ν_1/ν_3 (H_2S) or HS^- stretch	(3, 4, 5)
2427, 2323, 2285	2448, 2336, 2244,	2466, 2267	2407, 2315, 2232,	2445, 2345, 2234	2235	H_2S in NH_3/NH_4SH matrix	(5)
2042	2023	2032	2032	2024	2026	ν_2 (NH_4^+)+R (HS^-)[a]	(3, 4, 5)
1888	1863	1876	1864	1863	1866	ν_4 (NH_4^+)+R (HS^-)[a]	(3, 4, 5)
1710	1705	1706	1701	1701	1701	ν_2 (NH_4^+)	(3, 4, 5)
1625	1625	1625	1627	1625	1626	ν_4 (NH_3)	(1, 2)
1483	1475	1480	1477	1474	1476	ν_4 (NH_4^+)	(3, 4, 5)
1096	1104	1104	1109	1109	1109	ν_2 (NH_3)	(1, 2)

Notes.
[a] R: rotational lattice mode.
[b] References. (1) W. Zheng & R. I. Kaiser (2007); (2) J. S. Holt et al. (2004); (3) J. Bragin et al. (1977); (4) J. R. Ferraro et al. (1980); (5) K. Slavicinska et al. (2025).

Alternatively, the rapid proton transfer reaction between base and acid is also expected to take place,

$$NH_4^+ + HS^- \rightarrow NH_3 + H_2S. \quad (2)$$

In addition, NH_4^+ ions are expected to undergo decomposition with the formation of NH_3^+ and the hydrogen atom, similar to the isoelectronic methane (M. J. Abplanalp et al. 2018).

$$NH_4^+ \rightarrow NH_3^+ + H. \quad (3)$$

NH_3^+ can be retained in the processed ice matrix. All Reactions (1)–(3) lead to a rapid destruction of NH_4^+ in the initial period of ice irradiation (Figure 9(a)).

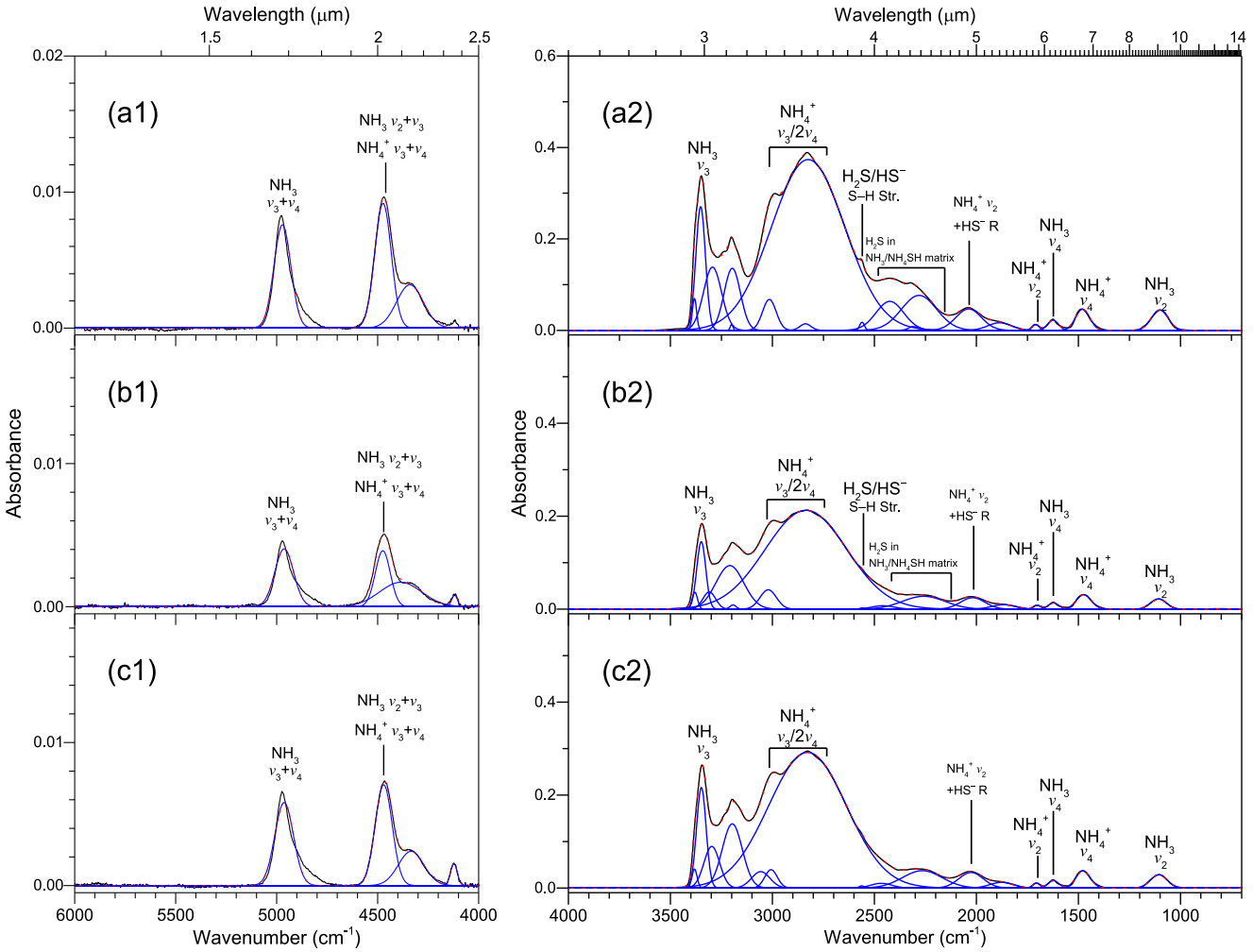

Figure 7. Infrared spectra of hydrogen sulfide and ammonia (H_2S-NH_3) ice mixtures. (a) before irradiation at 10 K, (b) after irradiation at 10 K, and (c) after irradiation at 10 K and then heating to 156 K. The experimental spectrum is plotted in black, while the deconvoluted peaks are blue, and their sum is shown with the dashed red line. Only noticeable peaks are labeled for clarity, and detailed peak assignments are listed in Table 3. The Str. and R indicate the stretch and rotational lattice mode.

Besides the aforementioned reactions, the NH_3 ice has been reported to generate products of hydrazine (N_2H_4), two N_2H_2 isomers ($HNNH/NNH_2$), molecular hydrogen (H_2), molecular nitrogen (N_2), hydrogen/ammonium azide (HN_3/NH_4N_3), triazane (N_3H_5), and the amino radical (NH_2) (W. Zheng et al. 2008; P. Parent et al. 2009; M. Forstel et al. 2015). Those of molecular products are also identified by the mass spectra, as shown in Figure 10. Hydrazine can be obtained through barrierless recombination of the amino radical (NH_2) from ammonia decomposition (Reactions (4) and (5)):

$$NH_3 \rightarrow NH_2 + H, \quad (4)$$

$$NH_2 + NH_2 \rightarrow N_2H_4. \quad (5)$$

However, because of the complex infrared features and the identical masses of ionized N_2H_4 and S in the mass spectrometer, along with the S^+ fragments from H_2S, it is too complicated to identify hydrazine in the mass spectrometer. The extended irradiation will lead to Reactions (6)–(10) of products of H_2, N_2, and N_2H_2 (W. Zheng et al. 2011) with the unimolecular dissociation induced by the impinging electrons,

$$N_2H_4 \rightarrow 2NH_2, \quad (6)$$

$$N_2H_4 \rightarrow N_2H_3 + H, \quad (7)$$

$$N_2H_3 \rightarrow N_2H_2 + H, \quad (8)$$

$$N_2H_2 \rightarrow N_2H + H, \quad (9)$$

$$N_2H \rightarrow N_2 + H. \quad (10)$$

For H_2S, when subject to irradiation, it can form sulfanyl (HS) and hydrogen (H) radicals, or atomic sulfur plus molecular hydrogen,

$$H_2S \rightarrow HS + H, \quad (11)$$

$$H_2S \rightarrow S + H_2. \quad (12)$$

The product H_2 can also contribute to the signals at $m/z = 2$ in Figure 10. At a low radiation dose, these species may subsequently form sulfanes (H_2S_n, $n \geqslant 2$) through barrierless radical recombination reactions or via insertion of sulfur atoms into a hydrogen–sulfur bond of the smaller sulfane molecules (Reactions (13)–(20)) (S. Cazaux et al. 2022; H. Carrascosa et al. 2024; A. Herath et al. 2025),

$$HS + HS \rightarrow H_2S_2, \quad (13)$$

$$H_2S_2 \rightarrow HS_2 + H, \quad (14)$$

$$HS + HS_2 \rightarrow H_2S_3, \quad (15)$$

$$HS + HS_n \rightarrow H_2S_{n+1}, \quad (16)$$

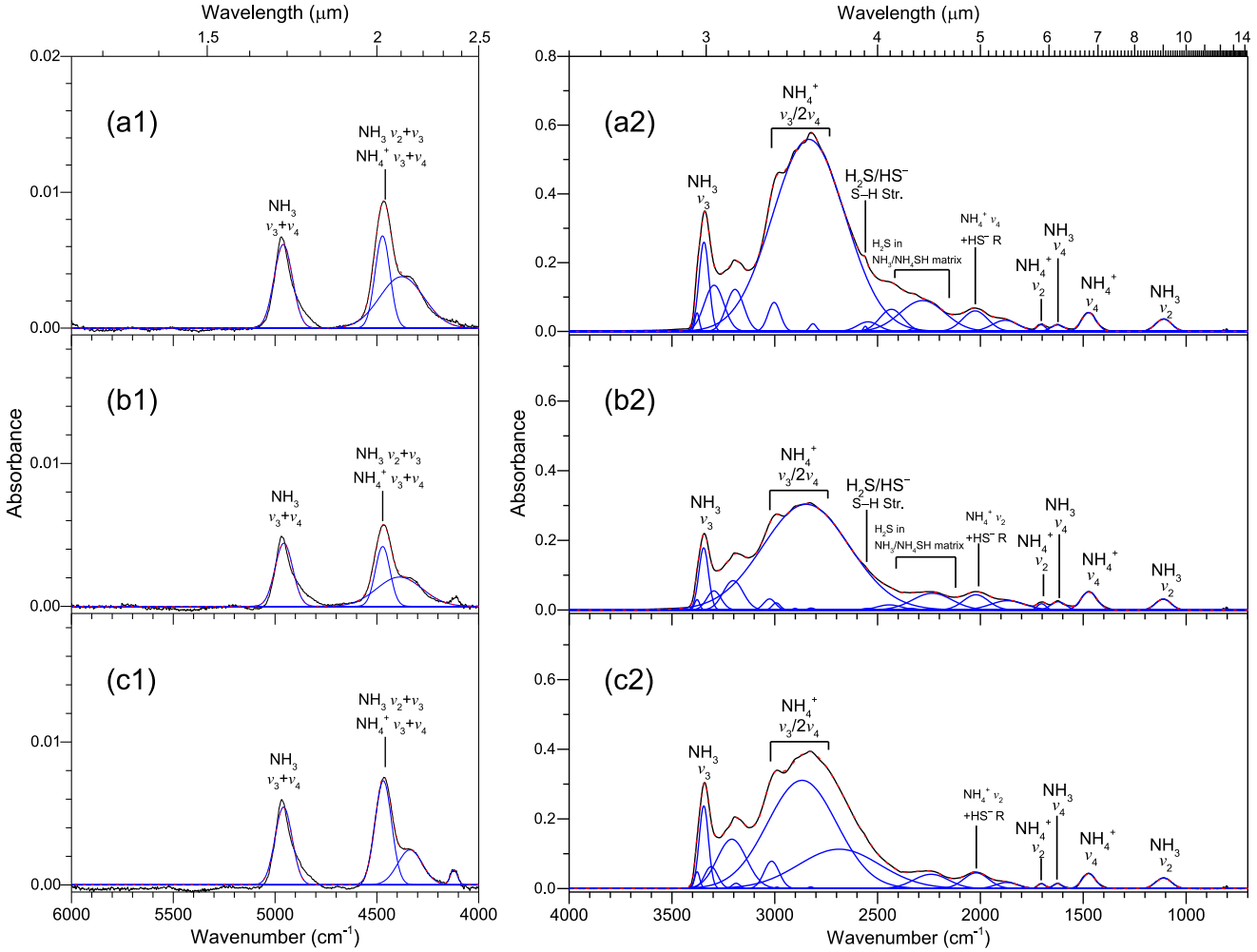

Figure 8. Infrared spectra of hydrogen sulfide and ammonia (H_2S-NH_3) ice mixtures. (a) before irradiation at 40 K, (b) after irradiation at 40 K, and (c) after irradiation at 40 K and then heating to 156 K. The experimental spectrum is plotted in black, while the deconvoluted peaks are blue, and their sum is shown with the dashed red line. Only noticeable peaks are labeled for clarity, and detailed peak assignments are listed in Table 3. The Str. and R indicate the stretch and rotational lattice mode.

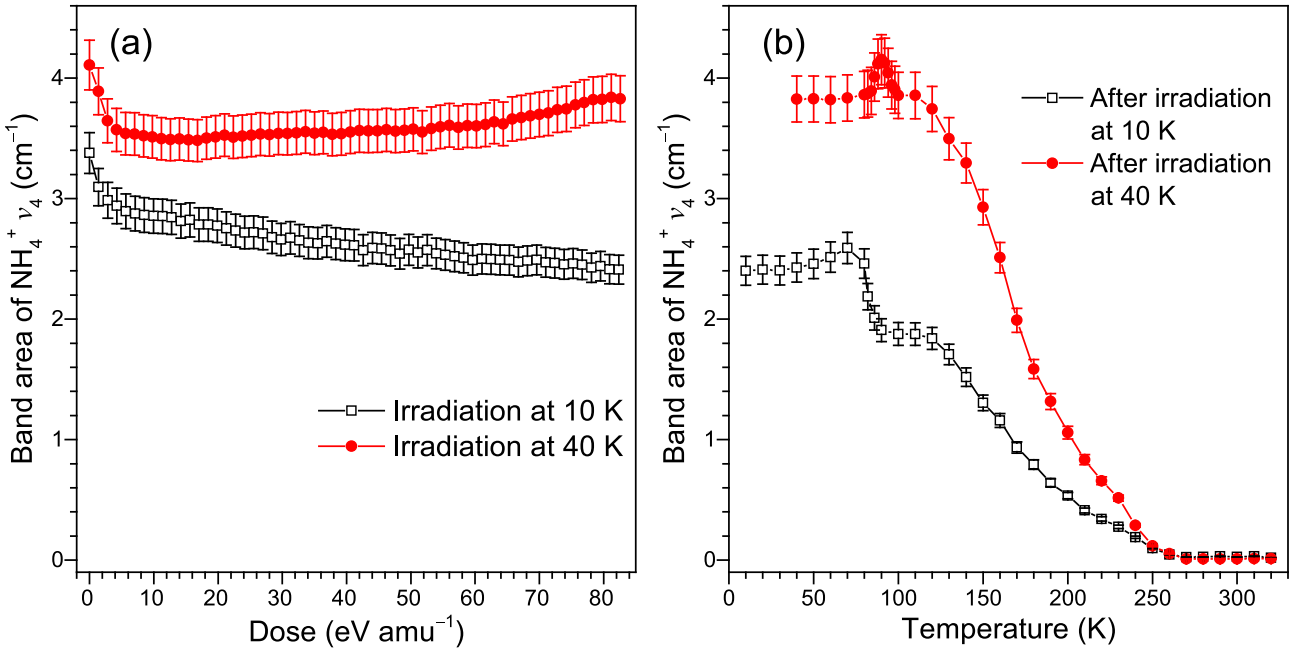

Figure 9. Areas of the ammonium (NH_4^+) ν_4 mode of the irradiated hydrogen sulfide and ammonia (H_2S–NH_3) ice mixtures. (a) During irradiation at 10 and 40 K. (b) During warm-up to 320 K.

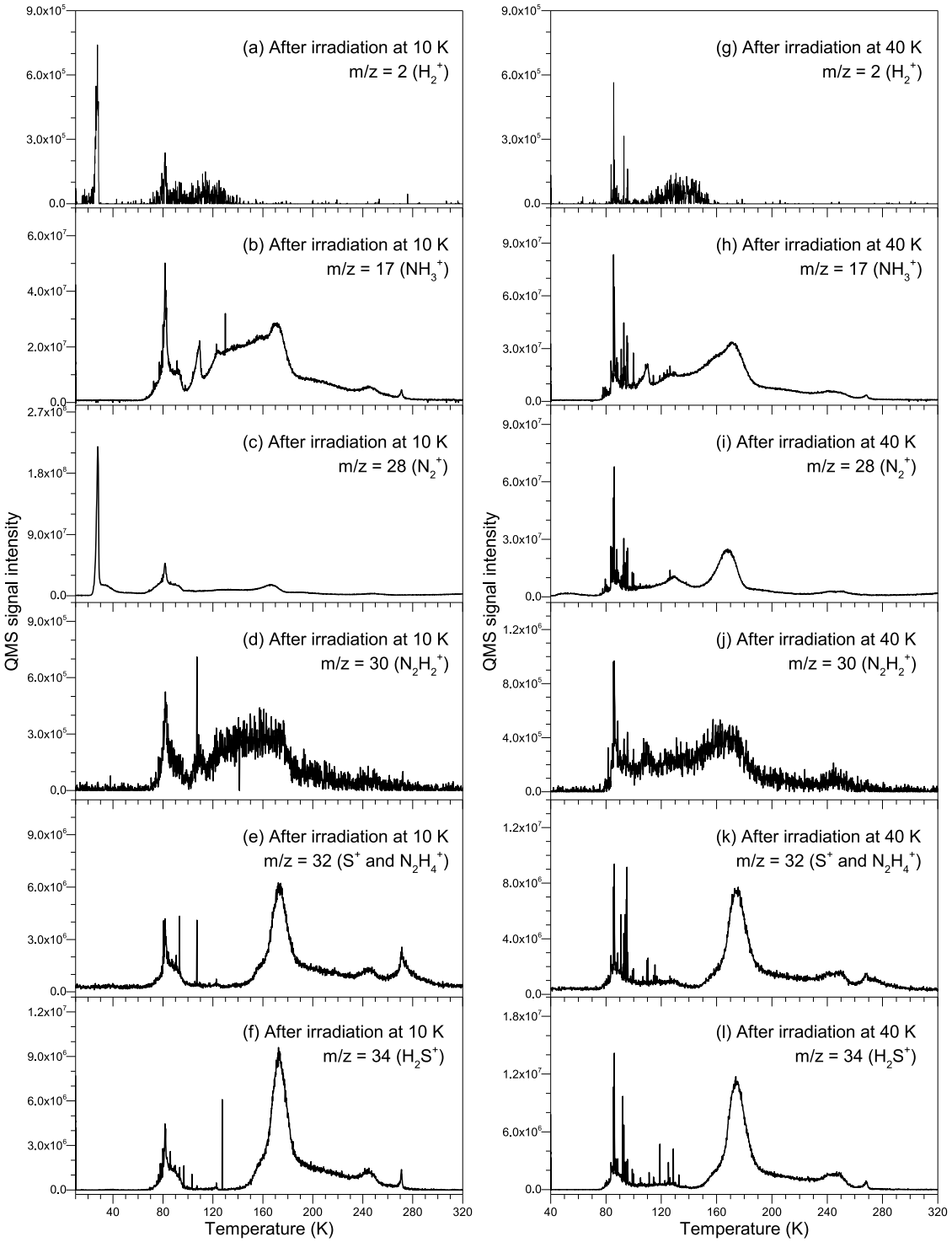

Figure 10. Quadrupole mass spectrometer (QMS) signals of mass to charge (m/z) at 2 (H_2^+), 17 (NH_3^+), 28 (N_2^+), 30 ($N_2H_2^+$), and 32 (S^+ and $N_2H_4^+$), and 34 (H_2S^+) during heating the irradiated hydrogen sulfide and ammonia (H_2S–NH_3) ice mixtures to 320 K from irradiated ices at 10 K (a)–(f) and 40 K (g)–(l).

$$HS_m + HS_n \rightarrow H_2S_{m+n}, \quad (17)$$

$$S + H_2S \rightarrow H_2S_2, \quad (18)$$

$$S + H_2S_2 \rightarrow H_2S_3, \quad (19)$$

$$S + H_2S_n \rightarrow H_2S_{n+1}. \quad (20)$$

For prolonged irradiation, intermediates like sulfur allotropes can be formed from the recombination of sulfur atoms and the dehydrogenation of sulfane molecules via Reactions (21) and (22),

$$S + S \rightarrow S_2, \quad (21)$$

$$S_m + S_n \rightarrow S_{m+n}, \quad (22)$$

where the cyclic octasulfur (S_8) has been reported as the most stable sulfur allotrope (B. Eckert & R. Steudel 2003). We collected the TPD profiles of molecules S_n (n = 2–8) and H_2S_n (n = 2–8) during heating the irradiated ices to 320 K, as shown

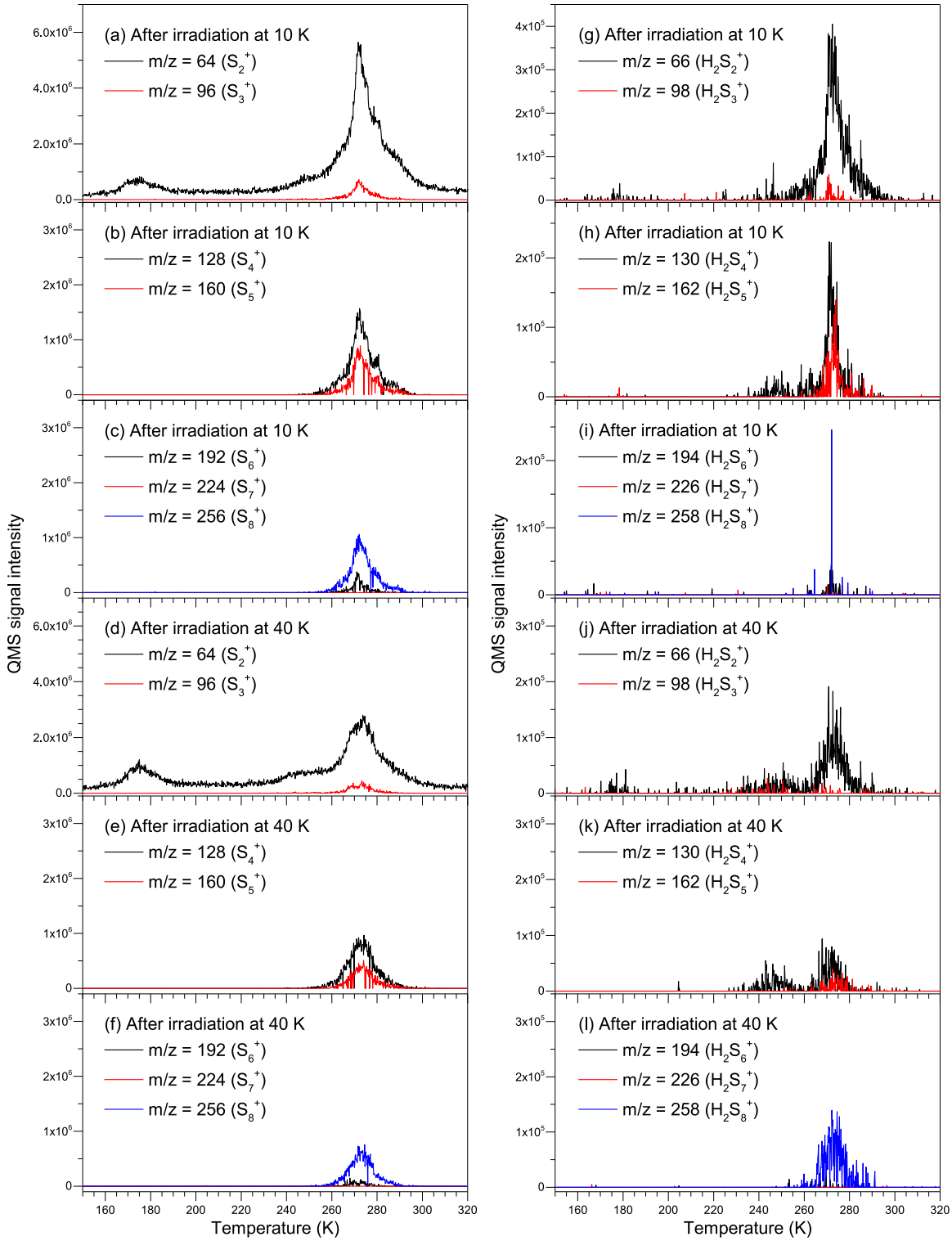

Figure 11. Quadrupole mass spectrometer (QMS) detection of sulfur-bearing fragments from high-order sulfane products during heating the irradiated hydrogen sulfide and ammonia (H_2S–NH_3) ice mixtures.

in Figure 11. For S_2, except for the cosublimation event with H_2S and NH_3, two peaks at 175 and 272 K are observed. The first peak agrees well with the detection of S_2 in the literature (H. Carrascosa et al. 2024; A. Herath et al. 2025), which was assigned to fragments originating from the molecule H_2S_3 (Z. Li et al. 2025). However, no sublimation event of H_2S_3 ($m/z = 98$) at this temperature is observed in this study. Surprisingly, all remaining molecules of S_n ($n = 2$–8) and H_2S_n ($n = 2$–8) present the same event at 272 K, suggesting fragments from sole parent compounds, i.e., higher-order sulfanes (H_2S_n, $n > 8$) (A. Herath et al. 2025). Apart from the primarily nitrogen-bearing or sulfur-bearing products, the molecules contain both of these atoms, like sulfur imide (SNH) and heptasulfur imide (S_7NH) (R. Steudel 1977;

X. Shao et al. 2025) are also expected to be formed, but the abundance of these products is too low, and more sensitive technologies like photoionization reflectron time-of-flight mass spectrometry may give further detailed information on their generation as well as the underlying formation mechanism.

4. Conclusions and Astrophysical Implications

In summary, we provide a systematic FTIR spectroscopy and mass spectrometry analysis of the NH_4SH salt formed from H_2S and NH_3 codeposition at cryogenic temperatures and during heating to 200 K, and exposed to ionizing radiation by the proxy of GCRs in the form of energetic electrons. The comparison between high-flux, high-temperature, and low-flux codeposition experiments suggests that the majority of observed NH_4SH salt in the ice mixtures is formed in the gas reaction before deposition on the low-temperature surface. During heating the mixed ices, infrared spectra found a new absorption peak at 1.98 μm (5053 cm^{-1}) correlating with crystalline NH_4SH with the crystallization process commencing at 136 K. Mass spectrometric analysis revealed that NH_4SH decomposed thermally to H_2S and NH_3 between 150 and 170 K. During irradiation of the ices, mass spectra indicated that the radiation chemistry of the NH_4SH salt yields a series of products, including hydrazine (N_2H_4), two N_2H_2 isomers ($HNNH/NNH_2$), molecular hydrogen (H_2), molecular nitrogen (N_2), and high-order sulfanes (H_2S_n, $n > 8$). After irradiation at 10 and 40 K, the evolution of the NH_4^+ ν_4 mode displays distinctly different behaviors when heated to 320 K, indicating a temperature-dependent radiation chemistry within the ice mixtures.

The volatile-loss model indicates that H_2S remains involatile in the trans-Neptunian regions and may be a crucial component in reddening the surfaces of TNOs (M. E. Brown et al. 2011; I. Wong & M. E. Brown 2016). This molecule is also proposed to be an essential reactant in producing molecular carriers for the 1.8 μm (~5555 cm^{-1}) band of Arrokoth and the weaker 3.9 μm (~2564 cm^{-1}) features in cliff-type TNOs (spectrally prominent organics) (W. M. Grundy et al. 2020; A. Mahjoub et al. 2021; R. Brunetto et al. 2025; B. J. Holler et al. 2025; N. Pinilla-Alonso et al. 2025). The presence of ammonia has been tentatively assigned on some TNOs like Charon and Orcus (M. A. Barucci et al. 2008a; M. E. Brown 2012). Under trans-Neptunian conditions, these two compositions can result in the formation of NH_4SH salt through a proton-transfer reaction, and the state of NH_4SH could provide valuable clues for interpreting astronomical observations of TNOs. First, the formation of NH_4SH salt on the surface of TNOs may offer an alternative explanation for the lack of detection of H_2S and the low abundance of NH_3 on some TNOs that was previously thought to be caused by the production of ammonia hydrate (C. M. Dalle Ore et al. 2019; P. D. Tribbett & M. J. Loeffler 2024). Second, the sulfur polymer products (S_x) from irradiated H_2S-bearing ice mixtures have been proposed to be key materials in reddening the color slopes of Io, Trojans, KBOs, and also the Great Red Spot of Jupiter (L. A. Lebofsky & M. B. Fegley 1976; J. R. Spencer et al. 1997; M. J. Loeffler et al. 2016; A. Mahjoub et al. 2017; M. J. Loeffler & R. L. Hudson 2018; M. J. Poston et al. 2018). But in the irradiated NH_4SH ices of this study, only high-order H_2S_n ($n > 8$) species are detected, while polysulfide species (S_x) are not identified. This suggests that NH_3 may partially counteract the reddening effect observed in irradiated H_2S-bearing ices. This behavior is similar to the effect found when NH_3 is added to carbon monoxide (CO) and methanol (CH_3OH), which reduces their color slopes during irradiation (C. Zhang et al. 2025a). Third, sulfur is the 10th most abundant element in the Universe, yet the issue of sulfur depletion in star-forming regions remains a topic of debate within the astrochemical community (D. P. Ruffle et al. 1999). The observed abundances of sulfur-bearing ices in interstellar environments, such as H_2S, SO_2, and OCS, are significantly lower than expected to explain the missing sulfur budget (A. Tieftrunk et al. 1994; T. Kushwahaa et al. 2023; M. K. McClure et al. 2023; W. R. M. Rocha et al. 2024). The formation of NH_4SH in interstellar environments, coupled with the generation of various complex sulfur-bearing compounds as a result of radiation chemistry (A. Jiménez-Escobar & G. M. Muñoz Caro 2011; A. Jiménez-Escobar et al. 2014; Y. J. Chen et al. 2015; J. Vitorino et al. 2024; A. Herath et al. 2025; K. Slavicinska et al. 2025), indicates that NH_4SH could play a crucial role in supplementing the incomplete sulfur inventory observed in the diffuse interstellar medium. Furthermore, the weaker 2.2 μm (~4545 cm^{-1}) band observed on the surface of Charon suggests the presence of ammonium ions (NH_4^+), which have been proposed to exist in the form of NH_4Cl (J. C. Cook et al. 2023). Since NH_4SH salt was found in high concentrations in the cometary grains of 67P (K. Altwegg et al. 2022)—a comet originating from the Kuiper Belt—it can be inferred that NH_4SH is likely widespread throughout the outer solar system. Consequently, it may also contribute to the 2.2 μm (~4545 cm^{-1}) spectral band of TNOs like Charon or Orcus. In addition, the extraterrestrial synthesis of NH_4SH occurs through the acid–base reaction characterized by a low or negligible energy barrier, which provides an alternative low-temperature route that can promote the complexity of space molecular formation. Therefore, studying the state of NH_4SH can significantly extend our understanding of complex chemical reactions in astrophysical scenarios where acid and base reactants, such as NH_3, HCN, HNCO, and HCOOH, are present (S. Raunier et al. 2003; F. Mispelaer et al. 2012; J. A. Noble et al. 2013; J. B. Bergner et al. 2016; F. Kruczkiewicz et al. 2021). This is particularly important for understanding the origin and evolution of ammonium ions (NH_4^+) detected in various extraterrestrial environments, including near young stellar objects and within cometary nuclei (W. A. Schutte & R. K. Khanna 2003; K. Altwegg et al. 2020; O. Poch et al. 2020; Z. M. Lewis et al. 2023; P. D. Tribbett & M. J. Loeffler 2024).

Acknowledgments

We acknowledge support from NASA grants 80NSSC24K1732.

Data Availability

The data behind the figures in this study are available in Zenodo at doi:10.5281/zenodo.20982728.

Appendix

The FTIR spectra of layered experiments are shown in Figure A1.

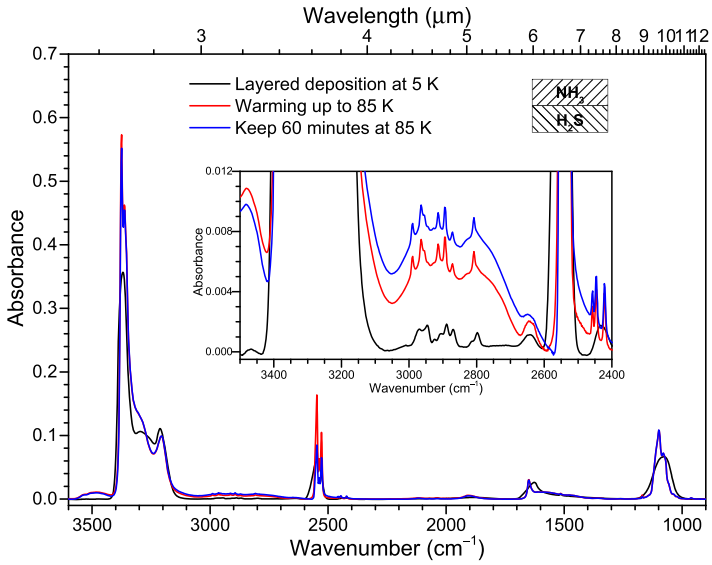

Figure A1. The selected infrared spectra from the layered experiments and the magnified view between the region of 3500–2400 cm^{-1}. The layered ice was obtained by first depositing H_2S and then NH_3 at the same vapor pressure. The thickness of this layered ice is controlled to be 850 ± 50 nm. At 85 K, the sublimation of H_2S and the formation of only a few products of NH_4SH indicate that the solid-state reaction responsible for producing NH_4SH is limited. At 85 K, crystallization of H_2S and NH_3 is also observed.

ORCID iDs

Chaojiang Zhang https://orcid.org/0000-0003-3727-901X
Jia Wang https://orcid.org/0000-0002-3795-8699
Leslie A. Young https://orcid.org/0000-0002-7547-3967
Ralf I. Kaiser https://orcid.org/0000-0002-7233-7206

References

Abplanalp, M. J., Förstel, M., & Kaiser, R. I. 2016, CPL, 644, 79
Abplanalp, M. J., Jones, B. M., & Kaiser, R. I. 2018, PCCP, 20, 5435
Altwegg, K., Balsiger, H., Hänni, N., et al. 2020, NatAs, 4, 533
Altwegg, K., Combi, M., Fuselier, S. A., et al. 2022, MNRAS, 516, 3900
Barucci, M. A., Brown, M. E., Emery, J. P., & Merlin, F. 2008a, in The Solar System Beyond Neptune, ed. M. A. Barucci, H. Boehnhardt, D. P. Cruikshank, & A. Morbidelli (Univ. Arizona Press), 143
Barucci, M. A., Merlin, F., Guilbert, A., et al. 2008b, A&A, 479, L13
Bennett, C. J., Ennis, C. P., & Kaiser, R. I. 2014, ApJ, 794, 57
Bennett, C. J., Jamieson, C. S., Osamura, Y., & Kaiser, R. I. 2005, ApJ, 624, 1097
Bennett, C. J., Pirim, C., & Orlando, T. M. 2013, ChRv, 113, 9086
Bergner, J. B., Öberg, K. I., Rajappan, M., & Fayolle, E. C. 2016, ApJ, 829, 85
Bragin, J., Diem, M., Guthals, D., & Chang, S. 1977, JChPh, 67, 1247
Brown, M. E. 2012, AREPS, 40, 467
Brown, M. E., Schaller, E. L., & Fraser, W. C. 2011, ApJL, 739, L60
Brunetto, R., Hénault, E., Cryan, S., et al. 2025, ApJL, 982, L8
Carrascosa, H., Muñoz Caro, G. M., Martín-Doménech, R., et al. 2024, MNRAS, 533, 967
Cazaux, S., Carrascosa, H., Muñoz Caro, G. M., et al. 2022, A&A, 657, A100
Chen, Y. J., Juang, K. J., Nuevo, M., et al. 2015, ApJ, 798, 80
Cook, J. C., Protopapa, S., Dalle Ore, C. M., et al. 2023, Icar, 389, 115242
Cooper, J. F., Christian, E. R., Richardson, J. D., & Wang, C. 2003, EM&P, 92, 261
Dalle Ore, C. M., Cruikshank, D. P., Protopapa, S., et al. 2019, SciA, 5, eaav5731
Drouin, D., Couture, A. R., Joly, D., et al. 2007, Scanning, 29, 92
Eckert, B., & Steudel, R. 2003, in Elemental Sulfur und Sulfur-Rich Compounds II, ed. R. Steudel (Springer), 31
Ferraro, J. R., Sill, G., & Fink, U. 1980, ApSpe, 34, 525
Forstel, M., Maksyutenko, P., Jones, B. M., et al. 2015, ChemPhysChem, 16, 3139
Goicoechea, J. R., Pety, J., Gerin, M., et al. 2006, A&A, 456, 565
Grundy, W. M., Bird, M. K., Britt, D. T., et al. 2020, Sci, 367, eaay3705
Heavens, O. S. 1955, Optical Properties of Thin Solid Films (1st ed.; Dover)
Herath, A., McAnally, M., Turner, A. M., et al. 2025, NatCo, 16, 5571
Holler, B. J., Brunetto, R., Cruikshank, D. P., et al. 2025, RNAAS, 9, 241
Holt, J. S., Sadoskas, D., & Pursell, C. J. 2004, JChPh, 120, 7153
Hudson, R., Palumbo, M. E., Strazzulla, G., et al. 2008, in The Solar System Beyond Neptune, ed. M. A. Barucci, H. Boehnhardt, D. P. Cruikshank, & A. Morbidelli (Univ. Arizona Press) , 507
Hudson, R. L., Gerakines, P. A., & Yarnall, Y. Y. 2022, ApJ, 925, 156
Jiménez-Escobar, A., & Muñoz Caro, G. M. 2011, A&A, 536, A91
Jiménez-Escobar, A., Muñoz Caro, G. M., & Chen, Y. J. 2014, MNRAS, 443, 343
Johnson, R. E. 1991, JGR, 96, 17553
Khare, B. N., & Sagan, C. 1971, Natur, 232, 577
Kruczkiewicz, F., Vitorino, J., Congiu, E., Theulé, P., & Dulieu, F. 2021, A&A, 652, A29
Kushwahaa, T., Drozdovskaya, M. N., Tychoniec, Ł., & Tabone, B. 2023, A&A, 672, A122
Lebofsky, L. A., & Fegley, M. B. 1976, Icar, 28, 379
Lewis, Z. M., Beth, A., Altwegg, K., et al. 2023, MNRAS, 523, 6208
Li, Z., Yang, J., Gong, X., et al. 2025, PCCP, 27, 5961
Loeffler, M. J., & Hudson, R. L. 2018, Icar, 302, 418
Loeffler, M. J., Hudson, R. L., Chanover, N. J., & Simon, A. A. 2015, Icar, 258, 181
Loeffler, M. J., Hudson, R. L., Chanover, N. J., & Simon, A. A. 2016, Icar, 271, 265
Luu, J. X., & Jewitt, D. C. 2002, ARA&A, 40, 63
Mahjoub, A., Brown, M. E., Poston, M. J., et al. 2021, ApJL, 914, L31
Mahjoub, A., Poston, M. J., Blacksberg, J., et al. 2017, ApJ, 846, 148
McClure, M. K., Rocha, W. R. M., Pontoppidan, K. M., et al. 2023, NatAs, 7, 431
Menten, S. M., Sori, M. M., & Bramson, A. M. 2022, NatCo, 13, 4457
Merlin, F., Barucci, M. A., de Bergh, C., et al. 2010, Icar, 210, 930
Mispelaer, F., Theule, P., Duvernay, F., Roubin, P., & Chiavassa, T. 2012, A&A, 540, A40
Niemann, H. B., Atreya, S. K., Carignan, G. R., et al. 1998, JGR, 103, 22831
Noble, J. A., Theule, P., Borget, F., et al. 2013, MNRAS, 428, 3262
Parent, Ph., Bournel, F., Lasne, J., et al. 2009, JChPh, 131, 154308
Parker, E. T., Cleaves, H. J., Dworkin, J. P., et al. 2011, PNAS, 108, 5526
Pinilla-Alonso, N., Brunetto, R., De Prá, M. N., et al. 2025, NatAs, 9, 230
Poch, O., Istiqomah, I., Quirico, E., et al. 2020, Sci, 367, eaaw7462
Poston, M. J., Mahjoub, A., Ehlmann, B. L., et al. 2018, ApJ, 856, 124
Quirico, E., Bacmann, A., Wolters, C., et al. 2023, Icar, 394, 115396
Raunier, S., Chiavassa, T., Marinelli, F., Allouche, A., & Aycard, J. P. 2003, CPL, 368, 594
Rocha, W. R. M., van Dishoeck, E. F., Ressler, M. E., et al. 2024, A&A, 683, A124
Ruffle, D. P., Hartquist, T. W., Caselli, P., & Williams, D. A. 1999, MNRAS, 306, 691
Schutte, W. A., & Khanna, R. K. 2003, A&A, 398, 1049
Shao, X., Jiang, J., Sun, B., et al. 2025, JAChS, 147, 31984

Slavicinska, K., Boogert, A. C. A., Tychoniec, Ł., et al. 2025, A&A, 693, A146
Spencer, J. R., McEwen, A. S., McGrath, M. A., et al. 1997, Icar, 127, 221
Steudel, R. 1977, JPhCh, 81, 343
Strazzulla, G., Cooper, J. F., Christian, E. R., & Johnson, R. E. 2003, CRPhy, 4, 791
Tieftrunk, A., Pineau des Forets, G., Schilke, P., & Walmsley, C. M. 1994, A&A, 289, 579
Tribbett, P. D., & Loeffler, M. J. 2024, PSJ, 5, 111
Turner, A. M., Abplanalp, M. J., Chen, S. Y., et al. 2015, PCCP, 17, 27281
Turner, A. M., Bergantini, A., Koutsogiannis, A. S., et al. 2021, ApJ, 916, 74
Turner, A. M., & Kaiser, R. I. 2020, AcChR, 53, 2791
Vitorino, J., Loison, J. C., Wakelam, V., Congiu, E., & Dulieu, F. 2024, MNRAS, 533, 52
Weidenschilling, S. J., & Lewis, J. S. 1973, Icar, 20, 465
Wong, I., & Brown, M. E. 2016, AJ, 152, 90
Wong, M. H., Mahaffy, P. R., Atreya, S. K., Niemann, H. B., & Owen, T. C. 2004, Icar, 171, 153
Yarnall, Y. Y., & Hudson, R. L. 2022, ApJL, 931, L4
Yeghikyan, A. 2017, Ap, 60, 374
Young, L. A., Braga-Ribas, F., & Johnson, R. E. 2020, in The Trans-Neptunian Solar System, ed. D. Prialnik, M. A. Barucci, & L. A. Young (Elsevier), 127
Zhang, C., Leyva, V., Wang, J., et al. 2024, PNAS, 121, e2320215121
Zhang, C., Wang, J., Turner, A. M., Young, L. A., & Kaiser, R. I. 2025a, ApJS, 278, 30
Zhang, C., Wang, J., Turner, A. M., Young, L. A., & Kaiser, R. I. 2025b, ApJS, 279, 1
Zheng, W., Jewitt, D., & Kaiser, R. I. 2009, JPCA, 113, 11174
Zheng, W., Jewitt, D., Osamura, Y., & Kaiser, R. I. 2008, ApJ, 674, 1242
Zheng, W., & Kaiser, R. I. 2007, CPL, 440, 229
Zheng, W., Kim, Y. S., & Kaiser, R. I. 2011, PCCP, 13, 15749